
Article:
Wheatcroft, L. orcid.org/0000-0003-2306-9791, Tran, T.D., Özkaya, D. et al. (2 more authors) (2022) Visualization of the delithiation mechanisms in high-voltage battery material LiCoPO4. ACS Applied Energy Materials, 5 (1). pp. 196-206. ISSN 2574-0962

https://doi.org/10.1021/acsaem.1c02742

Visualization of the Delithiation Mechanisms in High Voltage Battery Material $LiCoPO_4$

Laura Wheatcroft[a] *, Trung Dung Tran[b], Doğan Özkaya[b], James Cookson[b], Beverley J. Inkson[a]

[a] Department of Materials Science and Engineering, University of Sheffield, Mappin Street, Sheffield, S1 3JD, UK

[b] Johnson Matthey Technology Centre, Blounts Ct. Rd., Sonning Common, Reading, RG4 9NH, UK

ABSTRACT: $LiCoPO_4$ is a high voltage Li-ion battery material, seen as a potential candidate for electric vehicles due to its high energy density. However, $LiCoPO_4$ cathodes suffer from severe degradation on cycling. To date most $LiCoPO_4$ studies have involved bulk characterization techniques which do not allow the phases formed to be spatially resolved, thus information on which phases contribute to the severity of degradation, and reasons why, are lost. Here, the delithiation mechanisms of $LiCoPO_4$ are visualized by mapping changes in the valence state of Co across the electrode using *ex-situ* electron energy loss spectroscopy (EELS). To understand the effect of Co-O hybridization on $LiCoPO_4$ cyclability, changes in the O K-edge across the electrode during the first cycle, and later cycles were also mapped. Co-valence state EELS mapping showed lithium poor phases initially form on the outer edge of particles, corroborating a shrinking-core de-lithiation mechanism which was previously proposed from *in-situ* XRD. At higher potentials, the presence of Li-poor $CoPO_4$ correlates with Co-O bond hybridization, thus the instability of $CoPO_4$ leads to attack from the electrolyte and degradation at the electrode/ electrolyte interface. The instability of the de-lithiated phase results in Li re-incorporation at the surface at high potentials, shown by Co valence state EELS by Co(II)-rich regions forming on the surface of particles at high potentials. By the 10th cycle, $CoPO_4$ no longer forms, and capacity loss is caused by Li retention in the $LiCoPO_4$ lattice. The Co valence state EELS study reveals that strategies to improve the cyclability of $LiCoPO_4$ should focus on improving the stability of $CoPO_4$, or on methods to shield $CoPO_4$ from electrolyte degradation.

GRAPHICAL ABSTRACT

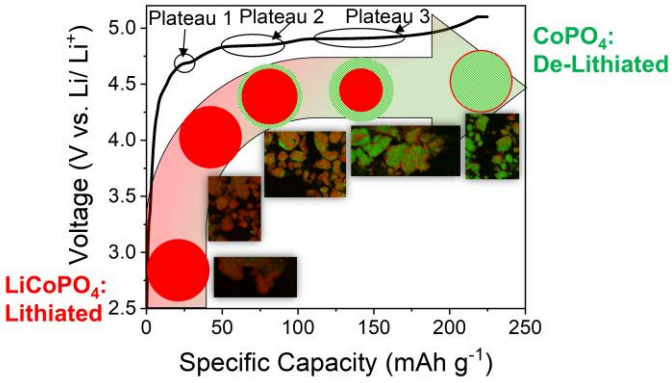

Key words: STEM-EELS, MLLS Fitting, Delithiation Mechanism, $LiCoPO_4$, High Voltage Battery Cathodes,

Introduction

High voltage Li-ion battery cathodes, with operating potentials greater than 4.5 V vs. Li/ Li^+, are being developed as a solution for electric vehicle batteries due to their potential for a high specific energy density [1,2]. $LiCoPO_4$ is a high voltage cathode developed in 2000 by Amine *et al.* [3]. $LiCoPO_4$ has a theoretical capacity of 167 mAh g^{-1}, coupled with a high nominal operating potential (4.8 V vs. Li/ Li^+) [3]. Despite the high cost of Co, the high operating potential, and theoretical capacity result in an overall cost per energy of the cell lower than other cathode materials [4], leading to significant interest in the development and optimization of $LiCoPO_4$ for electric vehicles.

Despite the potential advantages $LiCoPO_4$ offers for electric vehicles, to date $LiCoPO_4$ has not been successfully commercialized due to poor cyclability [4]. Poor cyclability results from structural instability in the electrode during cycling [5–8], and electrolyte induced degradation at the particle surface [9–11].

Understanding electrode de/lithiation mechanisms can aid understanding of degradation processes. Previous studies have focused on the phase transitions occurring in $LiCoPO_4$ [5–7]. $LiCoPO_4$ undergoes two phase transitions during delithiation: $LiCoPO_4 \rightarrow Li_{2/3}CoPO_4 \rightarrow CoPO_4$ [5,12,13]. The delithiated phase, $CoPO_4$, is known to be unstable due to octahedrally co-ordinated Co(III) being in a high spin state $(t_{2g})^4(e_g)^2$ which is energetically less favorable than the low spin state $(t_{2g})^6$ [5,13]. X-ray

absorption spectroscopy (XAS) studies of the electronic structure of $LiCoPO_4$ have found that the instability of $CoPO_4$ leads to mixed Co(II), and Co(III) oxidation states in delithiated $LiCoPO_4$. Hybridization of the Co-O bond due to O 2p hybridizing with transition metal 3d metal states has also been found at the delithiated $LiCoPO_4$ electrode surface [8]. The result of Co-O hybridization is potential O loss at the surface with progressive cycling.

The majority of $LiCoPO_4$ delithiation studies have involved non-spatially resolved techniques, such as X-ray diffraction (XRD) [5,6,12–14], or XAS [8]. Although XRD studies have indicated delithiation mechanisms involving coherent phase boundaries between the 3 phases within a single $LiCoPO_4$ particle based on peak asymmetry in XRD peaks of the nucleating phase with respect to the bulk phase[12,14], to date no study has spatially resolved the phases to identify the full delithiation mechanism. Understanding the spatial distribution of the stable and unstable phases could provide insight on methods to improve the cycle life of $LiCoPO_4$.

Mapping delithiation mechanisms is challenging due to difficulties detecting elemental lithium. Electron energy loss spectroscopy (EELS), a chemical characterization technique used in scanning transmission electron microscopy (STEM), has previously been used to map changes in the valence state of Fe in $LiFePO_4$ to map lithiation across $LiFePO_4$ particles [15]. During delithiation of $LiCoPO_4$ the valence state of Co changes from Co(II) → 2/3Co(II), 1/3Co(III) → Co(III) [5,13], so $LiCoPO_4$ is a candidate material for valence state mapping characterization.

In this study we use STEM-EELS Co valence state mapping (using the Co L-edge) to spatially resolve the phases forming during delithiation of $LiCoPO_4$, in order to understand the delithiation mechanisms. Evolution of the EELS O K-edge is also studied to understand the relative distribution of Co-O hybridization with respect to the phases formed during delithiation. Examination of the EELS Co L-edge, and O K-edge in electrodes after extended cycling is used to understand cathode microstructural changes resulting from increased cycle number.

Experimental

Cell Manufacture and Testing

$LiCoPO_4$ particles used here were coated in a 3-8 nm amorphous carbon coating (Johnson Matthey). Electrodes with a composition of 90 wt. % C-$LiCoPO_4$, 5 wt. % polyvinylidene fluoride (PVDF) binder (MTI), and 5 wt. % Super C65 carbon black conductive additive (C.Nergy TIMCAL) were manufactured using a tape casting method. A high active material loading (90 wt. %) was chosen to ensure a high concentration of active material for subsequent microstructural analysis. The solid material was mixed into a slurry using N-methyl-2-Pyrrolidone (Sigma Aldrich) as the solvent, and spread into a film of 200 µm thickness using a doctor blade. The film was dried at 80 °C, and the electrode calendared so the electrode density was between 1.8 and 2 g cm^{-3} to minimize inter-particle contact resistance.

The electrodes were assembled into 2016 stainless steel coin cells (MTI) using a 0.5 mm thick stainless steel spacer. Li metal (Sigma Aldrich) was used as the anode, with both a Whatman GF/ F fiber glass separator and a Celgard 2325 polypropylene-polyethylene-polypropylene separator. The Celgard separator was in contact with the electrode. 160 µL of $LiPF_6$ in a 50/50 volume ratio of ethylene carbonate (EC), and dimethyl carbonate (DMC) was used as the electrolyte.

The coin cells were galvanostatically cycled using a Maccor galvanostat at 0.1C after a 12-hour rest. The current density applied at 0.1C was calculated from the theoretical capacity of $LiCoPO_4$ (167 mAh g^{-1} [3,5]) and the active mass in the electrode.

For all the first cycle tests, the cells were galvanostatically cycled at 0.1C to different potentials up to 5.1 V vs. Li/ Li^+. At each stopping potential, the cells were held at the stopping potential for 30 mins to ensure equilibrium had been reached and reduce error incurred by post-mortem Li diffusion, whilst minimizing damage from adverse electrolyte reactions. The stopping potentials were chosen based on the position of peaks in the differential capacity curve.

For later cycle tests, the cells were cycled at 0.1C between 2.5 V vs. Li/ Li^+ and 5.1 V vs. Li/ Li^+. The cells were held at 5.1 V vs. Li/ Li^+ for 30 mins after each charge. The cells were rested for 1 hour after each discharge. Cycling was performed for 5 cycles, and 10 cycles, at which point significant capacity loss was observed. EELS characterization was performed on electrodes extracted from cells cycled to 5.1 V vs. Li/ Li^+ on the 10^{th} cycle. XRD was performed on cells cycled to 5.1 V vs. Li/ Li^+ on the 5^{th}, and 10^{th} cycles, and cells which had completed 5 and 10 cycles.

S/TEM Sample Preparation

To prepare the electrodes for *ex-situ* TEM and STEM-EELS characterization, the coin cells were de-crimped in an Ar filled glove box, and the electrodes washed in dimethyl carbonate. Slices of the electrode (~2 mm × 5 mm) were embedded into resin and cured at 65 °C for 3 days. The resin was prepared using 5 ml dodecenyl succinic anhydride (DDSA) (TAAB), 5 ml of araldite resin (CY212) (TAAB), and 5 drops of benzyldimethyl amine (BDMA) (TAAB). The electrodes were sectioned to 80 nm thickness into water using a Reichert-Jung Ultracut E ultramicrotome and a diamond blade and mounted onto Cu lacey carbon grids (EMR). Microtome sectioning was performed in order to (1) observe the cross-section of the $LiCoPO_4$ particles to better understand the phase distribution, and (2) reduce, and increase the homogeneity of, the sample thickness to reduce plural scattering effects during EELS collection [16].

After sectioning, the electrode samples were dried under vacuum for 24 hours, and stored in an Ar filled glove box until transport to the microscope to prevent further air exposure. The sections were sealed in Al-coated, Mylar bags under Ar for transportation. In total the electrodes were exposed to air for 30 s whilst mounting into resin, and 2 mins on transfer from the bags into the microscope. The effects of water exposure during microtoming and air exposure on the Co L-edge measurements are reported in the supplementary information.

STEM-EELS Oxidation State Characterization

STEM-EELS Oxidation State Data Collection

STEM-EELS characterization was performed at 200 kV with a JEOL JEM ARM200F. EELS spectrum images were collected using a Gatan Model 965 GIF Quantum ER spectrometer. High and low energy loss EELS spectra were collected simultaneously using Gatan's DualEELS capability to allow energy drift to be corrected by aligning spectrum images to the zero loss peak (ZLP). The total measurement time was between 5 and 10

mins for each spectrum image depending on the measurement area.

EELS Co L-edge spectrum images were measured by maximizing the energy resolution of the Co $L_{2,3}$-edge spectra. Spectra were obtained between 765 and 811 eV with an energy dispersion of 0.025 eV/ch achieving a ZLP full width half maximum (FWHM) of 0.475±0.025eV and a collection semi-angle, β, 55.5 mrad. The beam current, pixel sizes and dwell time were selected for low beam doses appropriate to avoid beam damage (based on our study of damage causing doses on uncycled $LiCoPO_4$). O K-edge spectrum images were collected using a 0.025 eV/ ch, or 0.1 eV/ ch (ZLP's FWHM = 0.7±0.1eV) energy dispersion.

STEM-EELS Oxidation State Data Processing

EELS results were processed using Gatan Microscopy Suite 3 (GMS3 Digital Micrograph). Prior to creating the Co valence state maps, the spectrum images were aligned to correct for energy drift so at each pixel, the zero loss peak occurred at 0 eV. The background was removed, and the signal was extracted using the power law background model.

Co valence state maps were created by fitting the Co L-edge spectra at each spectrum image pixel to Co(II), and Co(III)-rich L-edge standards using multiple linear least squares (MLLS) fitting. The ideal standards for MLLS fitting would be Co L-edges from fully discharged, and fully charged compounds- Co(II) from $LiCoPO_4$, and Co(III) from $CoPO_4$. The Co(II) standard was collected from uncycled $LiCoPO_4$. Pure $CoPO_4$ could not be synthesized by chemical delithiation, so the Co(III)-rich standard was collected from a $LiCoPO_4$ electrode charged to 5.1 V vs. Li/ Li^+, where selected area electron diffraction (SAED) and X-ray diffraction (XRD) confirmed the presence of $CoPO_4$ in 5.1 V vs. Li/ Li^+ charged electrodes.

The charged standard cannot be confirmed to be purely Co(III) as Li occupancy was not refined from the XRD, or SAED patterns. Therefore, the initial MLLS fitting was performed using a mixed Co oxidation state, and the Co(III) standard is referred to as Co(III)-rich. Details on the standards used in the MLLS fitting process are presented in the supplementary information.

Structural Characterization

Selected Area Electron Diffraction (SAED)

Ex-situ TEM imaging and SAED of the electrodes were performed using a JEOL JEM F200 at 200 kV with a Gatan One-View CCD.

X-ray Diffraction (XRD)

XRD patterns were collected using a Panalytical Empyrean diffractometer with a GalliPIX3D X-ray detector using Ag kα radiation to minimize fluorescence from the Co in $LiCoPO_4$. XRD patterns were collected in transmission mode using glass 0.5 mm diameter glass capillaries.

The samples were prepared for *ex-situ* XRD by washing the electrodes in dimethyl carbonate in an Ar filled glove box. The electrode material was scraped from the current collector, ground with a mortar and pestle and loaded in the glass capillaries in the glove box. The capillaries were sealed with wax to prevent air from contacting the electrode during pattern collection.

The XRD patterns were refined using Highscore software (Panalytical).

Results and Discussion

First Cycle: Electrochemical Characterization

In order to select appropriate potentials for *ex-situ* characterization of electrode phase changes, the electrochemical characteristics of $LiCoPO_4$ galvanostatically charged on the first cycle were analyzed (Figure *1*).

Figure *1*(a) is a representative galvanostatic charge curve at 0.1C of a $LiCoPO_4$ electrode. The specific capacity was calculated as the integral under the measured current against charging time curve, divided by the active mass of the electrode. Figure *1*(b) is the differential of capacity with respect to voltage of the galvanostatic charge curve in Figure *1*(a).

The first cycle total charging capacity is 223 mAh g^{-1}, which is larger than the theoretical capacity of $LiCoPO_4$ (167 mAh g^{-1} [3,12,17]) suggesting a contribution from electrolyte degradation [9,12]. The charging capacity typically only exceeds the theoretical capacity on the first charge.

3 plateaus are evident on the galvanostatic charge curve in Figure *1*(a) at 4.7, 4.8, and 4.9 V vs. Li/ Li^+, which correspond to peaks in the differential capacity curve in Figure *1*(b). The presence of plateaus at 4.8, and 4.9 V vs. Li/ Li^+ are consistent with other reported literature on $LiCoPO_4$ [5,12,14,17].

The specific capacities associated with the peaks in the differential capacity curve in Figure *1*(b) can be calculated by integrating under the peak and dividing by the active mass. The specific capacities associated with the peaks at 4.7, 4.8, and 4.9 V vs. Li/ Li^+ are 10, 55, and 86 mAh g^{-1} respectively.

The total capacity of the 2 larger peaks at 4.8, and 4.9 V vs. Li/ Li^+ is 151 mAh g^{-1}, less than the theoretical capacity (167 mAh g^{-1}), thus re-dox processes are responsible for the presence of peaks in the differential capacity curve in Figure *1*(b). Electrode microstructural characterization was performed after the completion of the charging plateaus at the points labelled on Figure *1*(a, and b) as these were the potentials where re-dox processes occur as per literature [5,6,14].

Due to differences in impedance between different electrodes, the voltage required to overcome the re-dox peaks in Figure *1* (b) differed slightly between electrodes. The overall aim of each *ex-situ* experiment was to stop charging after the completion of each peak on the differential capacity curve. Thus, XRD was performed on electrodes charged to 4.91 V vs. Li/ Li^+ as a complement to EELS results on an electrode charged to 4.89 V vs. Li/ Li^+. The second differential capacity peak had completed for both the 4.89 V vs. Li/ Li^+, and 4.91 V vs. Li/ Li^+ electrodes analyzed.

(a) 1st cycle 0.1C galvanostatic charge curve

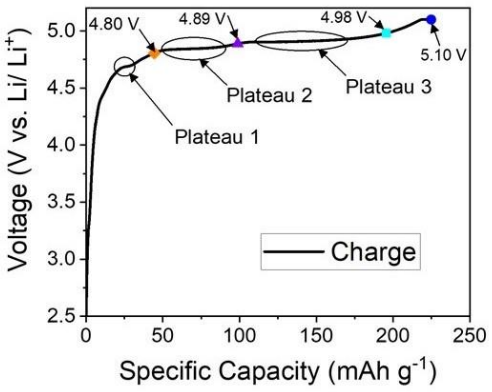

(b) 1st cycle 0.1C differential capacity curve

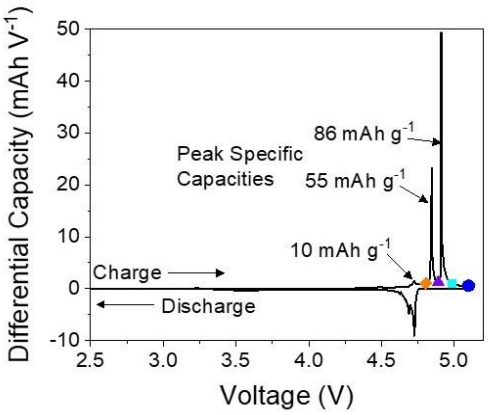

Figure 1: (a) Representative 0.1C galvanostatic charge curve of a $LiCoPO_4$ electrode on the first cycle. The 3 charging plateaus are labelled. (b) Representative differential capacity against voltage curve of the cell cycled in (a). The orange diamond, purple triangle, light blue square, and dark blue circle on the curves in (a) and (b) are the potentials at which STEM-EELS analyses of the electrodes were performed [18].

First Cycle: Bulk Structural Characterization

XRD

Ex-situ XRD was performed to confirm the phases present in the electrodes at the different charging potentials 4.91 V vs. Li/ Li^+ , 4.98 V vs. Li/ Li^+, and 5.1 V vs. Li/ Li^+ , occurring after the peaks in the differential capacity curve in Figure *1*(b). The XRD patterns in Figure *2* have been normalized by the (111) peak intensity (labelled).

Figure *2* shows that 3 phases form during delithiation (charging) of $LiCoPO_4$ electrodes, $LiCoPO_4$, $Li_{2/3}CoPO_4$, and $CoPO_4$ consistent with literature [5,14,17]. To identify and refine the phases, powder diffraction file (PDF) cards 01-089-6192, 04-014-7340, and 04-014-7341 from the ICDD were used for $LiCoPO_4$, $Li_{2/3}CoPO_4$, and $CoPO_4$ respectively. Li occupancy was not refined [18].

The XRD patterns in Figure *2* show that on delithiation of $LiCoPO_4$, the electrode remains in the $LiCoPO_4$ phase until 4.98 V vs. Li/ Li^+ (after the second differential capacity peak in Figure *1*(b)), after which the 2 phases $Li_{2/3}CoPO_4$ and $CoPO_4$ form and are detected at 4.98 V vs. Li/ Li^+. The lack of $Li_{2/3}CoPO_4$ at 4.91 V vs. Li/ Li^+ found here by *ex-situ* XRD is in contrast to *in-situ* XRD experiments by Palmer *et al.* [14] and Strobridge *et al.* [5,12] who found that reflections associated with the mid-phase $Li_{2/3}CoPO_4$ occur after the plateau at 4.8 V vs. Li/ Li^+ on the first cycle. This may imply $Li_{2/3}CoPO_4$ requires larger overpotentials to stabilize for *ex-situ* experiments.

Higher potentials at 5.10 V vs. Li/ Li^+ resulted in the formation of more $CoPO_4$, compared to 4.98V [18]. However, $Li_{2/3}CoPO_4$ was still present at 5.1 V vs. Li/ Li^+, indicating total delithiation of the electrode did not occur.

A peak at 4.7 V vs. Li/ Li^+ is present on the differential capacity curves in Figure *1*. No phase changes were observed at potentials lower than 4.98 V vs. Li/ Li^+ by XRD (Figure *2*), indicating the peak at 4.7 V vs. Li/ Li^+ did not result from a phase change [18]. Previous studies have suggested the first plateau results from a slight delithiation of the $LiCoPO_4$ lattice with no accompanying phase change, or electrolyte reactions[5].

All 3 phases present during charging of $LiCoPO_4$ maintain Pnma space group symmetry throughout delithiation. The phases differ by Li content, and unit cell dimensions. Full refinements of the uncycled electrode, and electrode charged to 5.1 V vs. Li/ Li^+ were performed on XRD patterns measured with a 1300 s dwell time, and are presented in the supplementary information. The refined unit cell dimensions of uncharged $LiCoPO_4$ were a= 10.203 Å, b= 5.920 Å, and c= 4.698 Å. The unit cell volume shrunk by 2.27 % during the phase change from $LiCoPO_4$ to $Li_{2/3}CoPO_4$, by compression in the a and b directions to a= 10.073 Å, and b= 5.853 Å, and expansion in the c direction to 4.704 Å. The largest shift in unit cell volume occurred when the phase changed from $Li_{2/3}CoPO_4$ to $CoPO_4$, with a further unit cell volume reduction of 5.08 %, coupled with further compression in the a and b direction (a=9.570 Å, and b=5.779 Å in $CoPO_4$), and a slight expansion in the c direction to 4.760 Å.

XRD patterns collected after charging $LiCoPO_4$ to different potentials on the first cycle

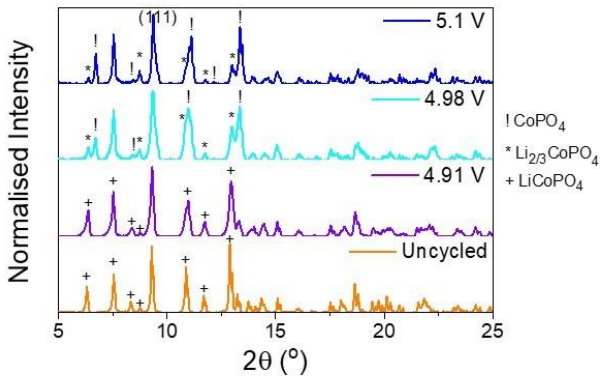

Figure 2: Ex-situ Ag Kα XRD patterns of an uncycled $LiCoPO_4$ electrode (orange), and electrodes galvanostatically charged at 0.1 C to 4.91 V (purple), 4.98 V (light blue), and 5.1 V (dark blue) vs. Li/ Li^+ on the first cycle. The XRD pattern intensities have been normalized by the (111) peak (labelled). High intensity reflections have been identified as originating from (!) $CoPO_4$, (*) $Li_{2/3}CoPO_4$, and (+) $LiCoPO_4$ [18].

First Cycle: S/TEM Characterization

Co L-edge Oxidation State Mapping

The phases present during charging of $LiCoPO_4$ found by XRD in Figure *2* indicate that the oxidation state of Co shifts from Co(II) to Co(III) on delithiation. EELS spectra of the Co L-edge were taken from an uncycled electrode, and an electrode charged on the first cycle to 5.1 V vs. Li/ Li^+ to confirm a Co oxidation state shift, and to determine standards for oxidation state mapping.

The Co L-edge spectra taken from the 5.1 V vs. Li/ Li^+ charged electrode were taken from Co(III)-rich regions found by MLLS fitting using CoO, and Co_3O_4 standards (see supplementary information) [18]. The ideal standards would have been the 3 phases present in $LiCoPO_4$ electrodes during charge ($LiCoPO_4$, $Li_{2/3}CoPO_4$, and $CoPO_4$). Unfortunately, $CoPO_4$ is thermodynamically unstable so this standard could not be acquired directly.

Co in Co_3O_4 is in a mixed (Co(II), Co(III)) oxidation state. As shown in the supplementary information, the Co L-edge of an oxide has very different characteristics compared with a phosphate. Therefore, mapping with Co-oxides as standards does not provide an accurate fitting to the data. However, the edge onset of the mixed oxide $Co_3(II, III)O_4$ is shifted to higher energy losses compared with Co(II)O, thus mapping with Co(II)O, and $Co_3(II, III)O_4$ provided an indication of which region of sample had the most extreme shift in Co L-edge onset.

Similar to $LiFePO_4$, the L_3 edge onset shifts to higher energy losses at higher oxidation states [15]. Only $CoPO_4$, and $Li_{2/3}CoPO_4$ were identified in the XRD pattern of the 5.1 V vs. Li/ Li^+ electrode (Figure *2*). Therefore, the Co L-edge shifted to the highest energy loss extracted in an electrode charged to 5.1 V vs. Li/ Li^+ is likely to represent the more de-lithiated Co(III)-rich regions, and was used as the Co(III) standard (see Figure *3*). As the Li content was not refined during XRD, the Co(III) standard in Figure *3* is defined as Co(III)-rich in the rest of this article.

The Co(II) edge in Figure *3* was a close fit to the Co L-edge of $Co_3(PO_4)_2$, a Co(II) phosphate (see supplementary information) [18]. Therefore, the L-edge extracted from the uncharged electrode is confirmed as a Co(II) standard.

The EELS spectra in Figure *3* show that as $LiCoPO_4$ delithiates, the Co L_3 edge peak shifts to a higher energy loss (780.9 eV on the uncycled electrode compared to 781.8 eV on the 5.1 V vs. Li/ Li^+ electrode), and the Co L_3 edge onset also shifts to higher energy losses on charging to 5.1 V vs. Li/ Li^+ (778.8 to 779 eV). Multiplets present on the Co L_2 and Co L_3-edges disappear on delithiation.

The changes in peak profile, the disappearance of the multiplets and shift in peak energy to higher energy loss values, are consistent with an increase in Co oxidation state, and are consistent with the XRD phase changes in Figure *2*. Previous XAS work by Lapping et al. [8] on $LiCoPO_4$ found that the presence of multiplets on $LiCoPO_4$ Co L-edges suggest a Co(II) oxidation state. Here, the lack of multiplets on the 5.1 V vs. Li/ Li^+ charged electrode Co EELS edge is consistent with it being Co(III)-rich. The characteristics of the Fe L-edge in $LiFePO_4$ are similar, with multiplets disappearing in the Fe(III) L-edge, and the Fe-L_3 peak shift shifting to higher energy losses [15]. Therefore, regions with EELS spectra which fit better to the Co(III)-rich standard represent the most de-lithiated phase found in the samples.

Co L-edge EELS spectra used as standards for MLLS fitting

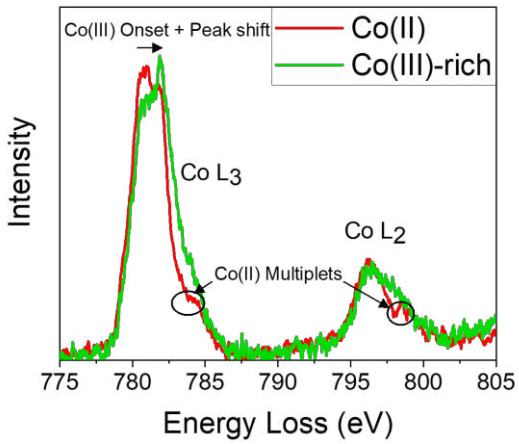

Figure 3: EELS spectra of the Co(II) (red) and Co(III)-rich (green) Co L-edge standards used for MLLS fitting taken at a 0.025 eV/ ch dispersion. The Co(II) standard was collected from an uncycled electrode. The Co(III)-rich standard was collected from a $LiCoPO_4$ electrode galvanostatically charged at 0.1C to 5.1 V vs. Li/ Li^+. The Co L_3- and Co L_2-edges are labelled. The position of the Co(II) multiplets are labelled on the Co(II) standard. The Co(III)-rich peak and edge-onsets shift to higher energy losses. The EELS spectra have been rescaled so the maxima on the Co L_3 edge have the same intensity [18].

A unique feature of studying the electronic structure of $LiCoPO_4$ using STEM-EELS, rather than bulk techniques such as XAS, is the ability to locally measure the electronic density of states within individual particles.

Using MLLS fitting and the Co(II), and Co(III)-rich standards in Figure *3*, the local distribution of Co(II), and Co(III)-rich regions could be imaged across particles charged to different voltages (Figure *4*) [18]. As the oxidation state shifts from Co(II) to Co(III)-rich during delithiation, the maps in Figure *4* are analogous to lithiation maps across the electrode.

The Co L-edges in Figure *3* were used as standards for MLLS fitting to map changes in Co oxidation state on spectrum images of an uncycled electrode, and electrodes charged to 4.8 V, 4.89 V, 4.98 V, and 5.1 V vs. Li/ Li^+ on the first cycle (*Figure 4*). Co(III)-rich areas (de-lithiated regions) are green on Figure *4*, and Co(II) areas (lithiated regions) are red on Figure *4*. The intensity of each pixel indicates how well the EELS spectrum at each pixel matched to the Co(III)-rich or Co(II) Co L-edge standards.

Cobalt oxidation state mapping was only done for Co(II) and Co(III)-rich regions as the mixed oxidation state $Li_{2/3}CoPO_4$ could not be reliably mapped because the Co L-edge was too similar to the Co(II) Co L-edge. As $Li_{2/3}CoPO_4$ is Co(II)-rich, areas rich in $Li_{2/3}CoPO_4$ appear red in the maps.

As expected by XRD (Figure *2*) and electrochemistry (Figure *1*), the uncycled and 4.8 V charged oxidation state maps are

mostly red Co(II)-rich (Figure *4*(b), and (d)), consistent with the particles being composed of $LiCoPO_4$.

Co(III)-rich (green regions) are present on the uncycled and 4.8 V vs. Li/ Li^+ maps, but these occur where the sample is thicker, seen as the brighter regions on the HAADF images in Figure *4*(a), and (c). In thick regions poor MLLS fitting occurs due to the change of background associated with multiple scattering. To reduce thickness-related errors, cycled samples were prepared for STEM-EELS analysis by microtoming[16] .

Co(III)-rich regions (green) start to form at 4.89 V vs. Li/ Li^+ on the edges of the particles (Figure *4*(f)), consistent with Li being extracted from the edges of particles. The Co(II)-rich regions of the 4.89 V vs. Li/ Li^+ particles also have a mixed oxidation state, consistent with partial delithiation, and potential presence of $Li_{2/3}CoPO_4$.

The presence of Co(III)-rich layers on the surface of 4.89 V vs. Li/ Li^+ particles was not consistent across every particle. It is likely that local differences in charge concentration due to the distribution of carbon black, or the local pore distribution, may have affected the homogeneity of the Co(III)-rich surface layer. The EELS mapping results found that particles closer to the current collector were more likely to remain Co(II) than those further away.

The presence of mixed Co(II) and Co(III)-rich regions at 4.89 V vs. Li/ Li^+ is consistent with the 4.8 V vs. Li/ Li^+ differential capacity peak in Figure *1*(b) being the $LiCoPO_4$ to $Li_{2/3}CoPO_4$ phase transition [5,6,12,14]. However, XRD in Figure *2* did not identify $Li_{2/3}CoPO_4$ being present at 4.89 V vs. Li/ Li^+. *Ex-situ* EELS and XRD were not performed on the exact same electrode. The results in Figure *4*(f) suggest $Li_{2/3}CoPO_4$ was present at levels undetectable by *ex-situ* XRD (a bulk-averaging technique) after passing the second peak on the differential capacity peak in Figure *1*(b).

The EELS mapping shows that at 4.98 V vs. Li/ Li^+ (Figure *4*(h)) the green Co(III)-rich regions extend further into the particles, leaving a Co(II) core. The presence of green Co(III), and red Co(II) oxidation states at 4.98 V vs. Li/ Li^+ is consistent with presence of $CoPO_4$, and $Li_{2/3}CoPO_4$ in the XRD patterns in Figure *2*. A red Co(II)-rich layer is also present at the surface of the particles (at the electrode/ electrolyte interface) (Figure *4*(h and j)). Thus EELS results are consistent with the 4.9 V vs. Li/ Li^+ differential capacity peak being the $Li_{2/3}CoPO_4 \rightarrow CoPO_4$ phase transition, corresponding to previous work[5,12,14,17,19].

By 5.1 V vs. Li/ Li^+ (Figure *4*(j)) the Co in the charged electrode is mostly Co(III)-rich, consistent with the presence of $CoPO_4$ identified by XRD in Figure *2*. The red Co(II)-rich region observed at 4.98 V vs. Li/ Li^+ on the surface of the charged particles is also present.

Co L-edge oxidation state maps on the first cycle

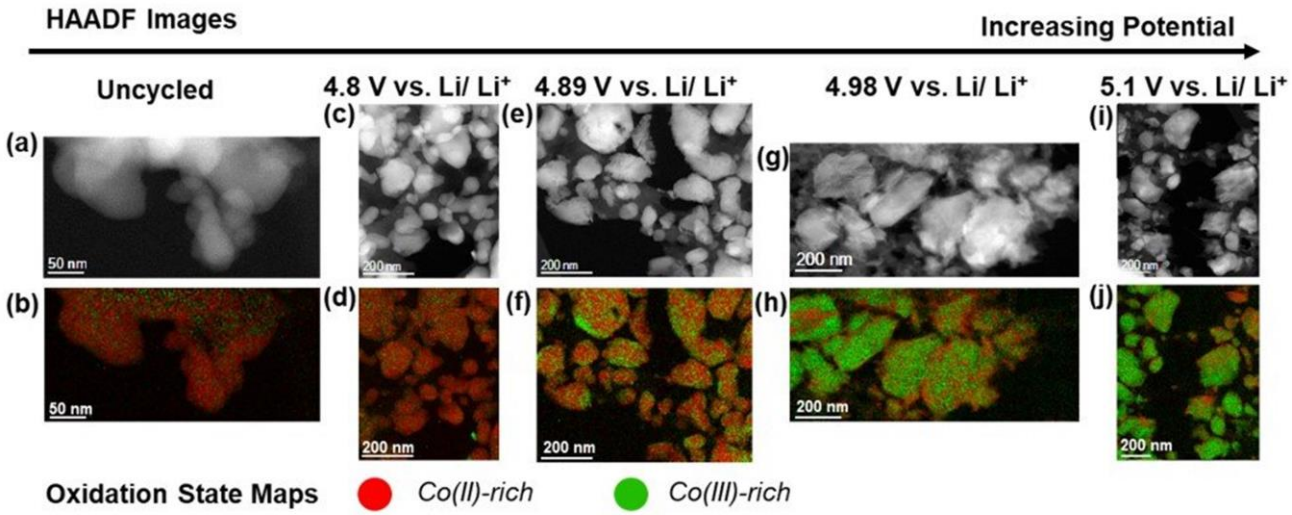

Figure 4: (a, c, e, g, and i) HAADF images, and (b, d, f, h, and j) the associated EELS Co L-edge oxidation state maps, of (a and b) an uncycled electrode, and electrodes charged at 0.1C on the first cycle to (c and d) 4.8 V vs. Li/ Li^+, (e and f) 4.89 V vs. Li/ Li^+, (g and h) 4.98 V vs. Li/ Li^+, and (i and j) 5.1 V vs. Li/ Li^+. Green regions in the Co oxidation state maps are Co(III)-rich oxidation state, and red regions are Co(II)-rich oxidation state [18].

The *ex-situ* post-mortem nature of the EELS mapping experiments performed here means the results presented in Figure *4* provide snapshots of the events occurring in the cell. There is also a possibility of ion distributions relaxing in the electrode after the application of voltage ceased, thus any meta-stable phases could relax to a more thermodynamically stable state. Despite this, the *ex-situ* EELS transition metal valence mapping technique has been previously performed on $LiFePO_4$ to identify lithiation mechanisms *ex-situ* [15,20]. The initial formation of Co(III)-rich regions on the edges of particles at 4.89 V vs. Li/ Li^+ (Figure *4* (f)) implies that de-lithiated regions of material initially form on the edge of particles. Eventually Co(II)-rich

cores form in particles at higher concentrations (see Figure *4* (h)), suggesting Li has been extracted from the outside of the particles, leaving a Li-rich center. It should be noted that the appearance of the Co(III)-rich regions on the outside of particles at 4.89 V vs. Li/ Li^+ in Figure *4* (f) is not consistent across every particle. The inconsistency is likely due to localized differences in impedance across the electrode meaning de-lithiation varies between particles.

Although the exact de-lithiation mechanism cannot be conclusively confirmed due to the postmortem 'snap-shot' nature of the *ex-situ* experiments, the formation of lithium poor regions on the outer surface of particles, and eventual formation of a Li-rich core (demonstrated in Figure *4* (f), and (h)) corroborates a shrinking-core de-lithiation mechanisms initially proposed by Palmer *et al.* for $LiCoPO_4$ using *in-situ* XRD [14]. A schematic of a potential shrinking-core mechanism is shown in Figure 5.

At high potentials (4.98, and 5.1 V vs. Li/ Li^+), a Co(II)-rich layer is observed to form on the edge of delithiated particles (*Figure 4 (h) and (j)*). A Co(II)-rich outer surface layer has previously been observed by Lapping *et al.* using XAS [8], and is consistent with Li re-incorporation at the surface due to an unstable cathode electrolyte interphase (CEI)-type [21]. 4.98 and 5.1 V vs. Li/ Li^+ are both above the breakdown potential of the LP-30 electrolyte, and CEI layers have been previously reported on $LiCoPO_4$ electrodes at these potentials [21]. Manzi *et al.* previously reported a spontaneous re-incorporation of Li at high potentials due to Co(III) in $CoPO_4$ spontaneously reacting with alkyl carbonates in F-containing electrolytes which would result in a reduction of Co(III) to Co (II) at the surface [11].

The Co(II)-rich surface feature is not consistent across all particles in Figure *4*(h) and (j). Our previous work imaging CEI layers on $LiCoPO_4$ with helium ion microscopy demonstrated that CEI layers on $LiCoPO_4$ form with inhomogeneous thickness variations, and are unstable [21]. The inconsistency in the Co(II)-rich layer could have arisen due to an inhomogeneous CEI. However, it was not possible to verify the CEI inhomogeneity here due to the microtome sample preparation destroying any CEI.

Overall, the results here corroborate a shrinking-core mechanism proposed previously by Palmer *et al.* [14]. The added spatial sensitivity of the EELS valence technique suggests Li re-incorporation at higher potentials as a result of electrolyte attack. The EELS technique also shows the spatial distribution of the Co(III)-rich and Co(II) rich regions and effect of inhomogeneities within the electrode on electrochemical activity.

Schematic of a potential $LiCoPO_4$ delithiation mechanism

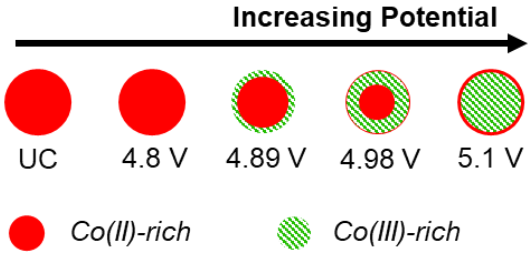

Figure 5: Schematic of the proposed shrinking-core delithiation mechanism experienced by $LiCoPO_4$ at increasing potentials, V vs. Li/ Li^+. Red= Co(II)-rich, and green-striped= Co(III)-rich.

O K-edge

To check if O was also redox active, EELS spectra of the O K-edge were also taken (Figure *6*). The EELS mapping technique enabled the changes in the O K-edge to be spatially correlated with changes in the Co L-edge. The O K-edges in Figure *6* were extracted from Co(II)-rich areas on an uncycled electrode (red), and Co(III)-rich areas on an electrode charged to 5.1 V vs. Li/ Li^+ (green).

The O K-edges extracted from the Co(II), and Co(III)-rich regions have a similar shape. The O K-edge spectra in Figure *6* were deconvolved using the Fourier-ratio method as the presence of C in the electrode caused the effects of plural scattering to be worse at the O K-edge due to the proximity of the O K-edge to the C-K edge.

A pre-edge feature occurs at 533.3 eV on the Co(III)-rich region extracted O K-edge in Figure *6*. The pre-edge is consistent with O-2p hybridization with empty Co 3d states when Co is in the 3+ oxidation state [8]. O K-edge XAS measurements of $LiCoPO_4$ have previously measured Co-O hybridization of the O 2p states with the Co 3d states [8].

O K-edge EELS spectra collected on the first cycle

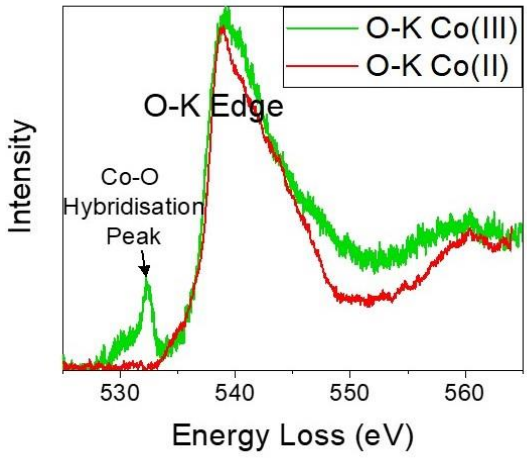

Figure 6: EELS spectra of the O K-edge taken at a 0.025 eV/ ch dispersion extracted from Co(II)-rich regions (red) of an uncycled $LiCoPO_4$ electrode, and Co(III)-rich regions (green) of a 5.1 V vs. Li/ Li^+ electrode. The O K-edge, and Co-O hybridization pre-edge feature are labelled. The EELS spectra have been rescaled so the maxima on the O K-edge edge have the same intensity [18].

To confirm that the presence of the hybridization pre-edge was directly correlated with the presence of Co(III)-rich regions across the charged electrode, O K-edge maps (Figure *7*(c)) were created with the O K-edge standards in Figure *6*, and compared with Co L-edge oxidation state maps (Figure *7*(b)) in an electrode charged to 5.1 V vs. Li/ Li^+ (Figure *7*) [18]. In the sample examined, Co(II)-rich regions were still present at the center of the particles surrounded by Co(III)-rich regions on the outside of particles, similar to the 4.98 V vs. Li/ Li^+ charged electrode shown in *Figure 4*(h).

Comparing the distribution of Co(II)/Co(III) oxidation states within two different electrodes charged to 5.1 V vs. Li/ Li^+ on the first cycle, the proportion of Co(II)-rich regions remaining is higher in the particles mapped in Figure *7*(b) compared with sample Figure *4*(j). Provisional mapping of electrodes cross-sectioned by microtome suggested that particles positioned closer to the current collector (further from the anode) were more likely to be Co(II)-rich in electrodes charged to 5.1 V vs. Li/ Li^+.

Correlating the distribution of the Co oxidation states and the oxygen hybridization using comparative EELS maps in Figure *7*, the O K-edge pre-edge feature distribution broadly matches the Co(III)-rich distribution, showing that the EELS hybridization pre-edge is a feature of Co(III)-rich regions of delithiated $LiCoPO_4$ particles. This is likely due to extra density of states available in the Co(III) configuration for hybridization (O-2p-Co-3d), as explored using DFT modelling by Lapping *et al.* [8]. Hence the EELS analysis shows that O is also redox active in $LiCoPO_4$ at high potentials (above 4.9 V vs. Li/ Li^+).

It should be noted that the O K-edge spectrum image in Figure *7*(c) is noisier than the Co L-edge. Due to the comparatively low intensity nature of the O K-edge pre-edge (see Figure *11*), the pre-edge signal in the EELS spectra at each individual pixel was noisier than the Co L-edge features, resulting in a poorer O K-edge fit than for the Co L-edge.

EELS spectrum images of delithiated $LiCoPO_4$ particles showing Co(III)-rich regions match regions which have a Co-O hybridization pre-edge on the O K-edge.

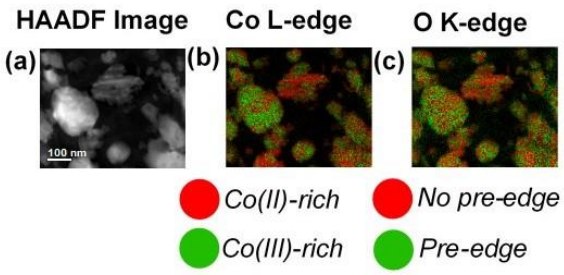

Figure 7: (a) HAADF image, and the associated EELS (b) Co L-edge oxidation state map, and (c) O K-edge map, of an $LiCoPO_4$ electrode charged to 5.1 V vs. Li/ Li^+ on the first cycle. Green regions on the Co L-edge map in (b) are Co(III)-rich, and red regions are Co(II)-rich. Green regions on the O K-edge map (c) have been fit to the O K-edge standard with the Co-O hybridization pre-edge in Figure 6, and red regions have been fit to the O K-edge standard with no pre-edge feature (Figure 6) [18].

First Cycle: Structural Imaging and SAED

To investigate if the observed changes in Co oxidation state correlated with structural change in the charged $LiCoPO_4$ electrode particles, high resolution TEM (HRTEM) imaging [18], and SAED were performed on microtomed samples (Figure *8*). The amorphous carbon coating is visible on the TEM image of the edge of a 4.89 V vs. Li/ Li^+ charged particle in Figure *8*(a). EELS C K-edge mapping of the carbon layer on a pristine $LiCoPO_4$ particle is shown in the supplementary information.

HRTEM imaging of $LiCoPO_4$ electrode particles charged to 4.89 V vs. Li/ Li^+ shows a 3 nm surface layer underneath the amorphous carbon coating with different contrast to the bulk of the particle. SAED of the inner cores of particles charged to 4.89 V vs. Li/ Li^+ confirmed the presence of $LiCoPO_4$, consistent with XRD in Figure *2*. The presence of an outer layer on the surface correlates with the location of an observed Co(III)-rich region on the surface of 4.89 V vs. Li/ Li^+ charged particles in Figure *4*(f). This is likely due to preferential delithiation from the edges of the particles, consistent with the shrinking-core delithiation mechanism outlined in *Figure 5*.

Figure *8*(b) shows a 5.1V vs. Li/ Li^+ charged particle imaged by HRTEM down a [1 -2 3] zone axis. The particle was identified from SAED as $Li_{2/3}CoPO_4$, and other regions indexed on the same electrode sample were found to be $CoPO_4$ (see supplementary information). The exact position of the particle relative to the current collector is unknown, so the particle may have been located further from the anode (in a more lithiated region) than the particles measured using EELS (*Figure 4 (j)*).

Using HRTEM imaging it is difficult to distinguish phase transitions and the location of the interfaces between $LiCoPO_4$, $Li_{2/3}CoPO_4$, and $CoPO_4$, by changes in lattice spacing as the differences in unit cell sizes, and hence lattice fringe spacings, are small. The potential growth of a surface layer of $Li_{2/3}CoPO_4$ on the particle in *Figure 8*(a) would only result in a 2.27 % unit cell volume shrinkage from $LiCoPO_4$ to $Li_{2/3}CoPO_4$ (from XRD in Figure *2*), and measureable changes in fringe spacing are not apparent (*Figure 8* (a)). A surface layer is also not apparent on the 5.1 V vs. Li/ Li^+ particle (*Figure 8* (b)) for similar reasons.

For the particles imaged by HRTEM (Figure *8*), the lattice contrast is maintained between the bulk and the surface layers on both Figure *8*(a) and (b), consistent with all 3 phases present during charging maintaining Pnma crystal symmetry. The continuation of the atomic layers, also indicates that the interfaces between phases present in the particles in Figure *8* are predominantly coherent, consistent with XRD analysis by Strobridge *et al.* [5].

(a) Surface layer formation at 4.89 V vs. Li/ Li$^+$

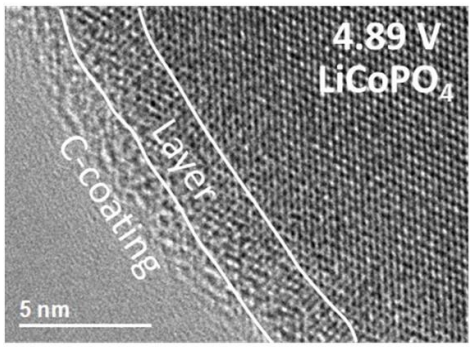

(b) Surface layer formation at 5.1 V vs. Li/ Li$^+$

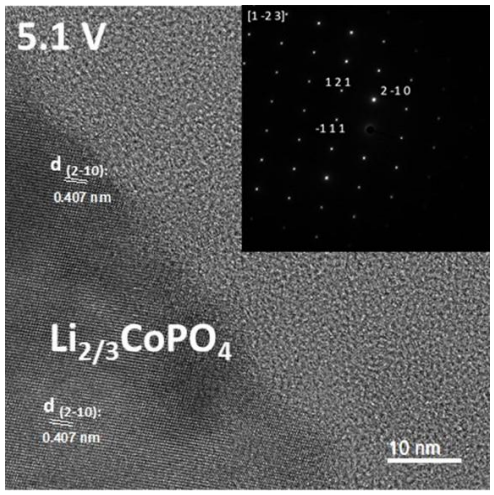

Figure 8: TEM images of (a) edge of a $LiCoPO_4$ particle charged to 4.89 V vs. Li/ Li$^+$ showing a surface layer beneath the carbon coating, and (b) the edge of a particle charged to 5.1 V vs. Li/ Li$^+$ and the associated $Li_{2/3}CoPO_4$ [1-23]$_{ZA}$ SAED pattern [18].

Later Cycles: Electrochemical Characterization

The $LiCoPO_4$ cells cycled here suffered severe capacity loss after 10 cycles (128 mAh g^{-1}- 14 mAh g^{-1}). To examine the evolution of electrochemical behavior with cycle number, the charging differential capacity curves of cycle 1, 5, and 10 are compared (Figure *9*) [18].

The first cycle differential capacity curve in Figure *9* is from the same sample as in Figure *1*(b) with 3 peaks at 4.7, 4.8, and 4.9 V vs. Li/ Li$^+$. Comparison of the differential capacity curves in Figure *9* shows that after 5 cycles, 2 peaks at 4.8 V vs. Li/ Li$^+$, and 4.95 V vs. Li/ Li$^+$ are present, but with lower gravimetric capacities than the peaks on the first cycle (28 mAh g^{-1}, and 38 mAh g^{-1} respectively). Assuming these two peaks represent the capacity gained by delithiation of $LiCoPO_4$, the relative contribution of the 4.8 V vs. Li/ Li$^+$ peak to the delithiation of remaining active $LiCoPO_4$ ($LiCoPO_4 \rightarrow Li_{2/3}CoPO_4$) is similar, being 39% 1st cycle and 38% 5th cycle. The relative contributions 39%, and 38 % were calculated by the peak specific capacity divided by the sum of the specific capacities of the two peaks.

For the fifth cycle differential capacity curve (Figure *9*), it is unclear why the highest voltage capacity peak occurs at a higher potential on the 5th cycle (4.95 V vs. Li/ Li$^+$) compared to the 1st cycle (4.9 V vs. Li/ Li$^+$) in Figure *9*, but the discrepancy may be due to differences in impedance between different electrodes.

After 10 cycles, peaks in the differential capacity curve in Figure *9* are no longer evident.

Differential capacity curves at different cycle numbers

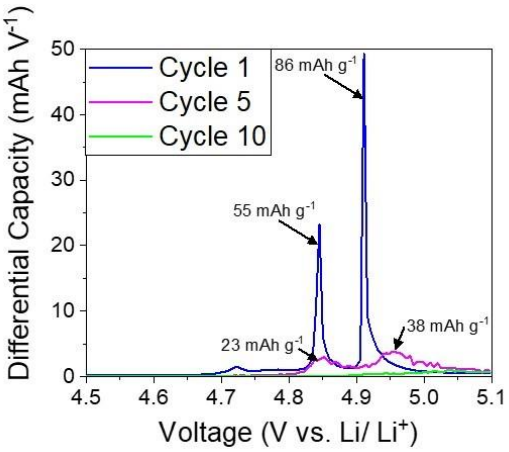

Figure 9: Differential capacity against voltage curves for $LiCoPO_4$ electrodes charged to 5.1 V vs. Li/ Li$^+$ at 0.1C on the 1st cycle (blue), 5th cycle (pink), and 10th cycle (green). The specific capacities calculated from the area under the large differential capacity peaks for the 1st and 5th cycles are shown on the graph [18].

Later Cycles: Bulk Structural Characterization

XRD

Ex-situ XRD patterns were taken of electrodes charged to 5.1 V vs. Li/ Li$^+$ after 1, 5, and 10 cycles, and compared to an uncycled electrode (Figure *10*) to confirm which phases are present. Figure *10* shows that $CoPO_4$, and $Li_{2/3}CoPO_4$ are present after charging to 5.1 V vs. Li/ Li$^+$ on the 1st and 5th cycles. Under these conditions, the presence of $CoPO_4$, (Figure *10*) indicates that the electrodes were redox active at the 1st and 5th cycles.

Phase proportions were calculated from the XRD patterns in Figure *10*. The relative proportion of $CoPO_4$ found in electrodes charged to 5.1 V vs. Li/ Li$^+$ decreased from 58.1 % at the 1st cycle to 15. 6 % by the 5th cycle. Less $CoPO_4$ at 5.1 V vs. Li/ Li$^+$ on the 5th cycle is consistent with the loss in capacity by the 5th cycle.

By the 10th cycle no $CoPO_4$, or $Li_{2/3}CoPO_4$ were detected in the charged electrode samples by XRD, only residual $LiCoPO_4$ (see Figure *10*). The lack of measureable $CoPO_4$ and $Li_{2/3}CoPO_4$ is consistent with the lack of peaks in the differential capacity curve in Figure *9* by the 10^{th,} cycle indicating severe curtailment of the desirable delithiation phase transformations. An issue with *ex-situ* methods is self-discharge can occur between cycling and decrimping[11], which may account for the lack of measured $CoPO_4$ and $Li_{2/3}CoPO_4$ despite a small observable discharge capacity (14 mAh g^{-1}). It is likely the proportion of $CoPO_4$, and $Li_{2/3}CoPO_4$ was simply too small to be observed by XRD by the 10th cycle.

XRD patterns collected at different cycles

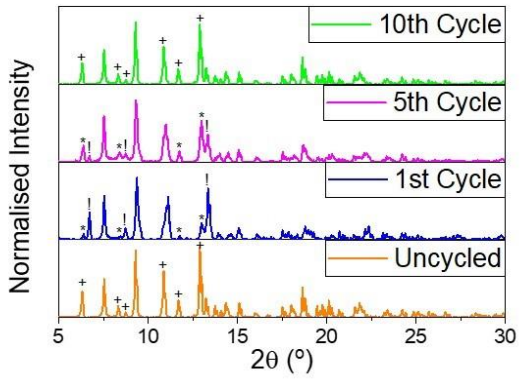

Figure 10: Ag kα XRD patterns of an uncycled $LiCoPO_4$ electrode (orange), and $LiCoPO_4$ electrodes charged to 5.1 V vs. Li/ Li^+ on the 1st cycle (blue), 5th cycle (pink), and 10th cycle (green). High intensity reflections have been identified as originating from (!) $CoPO_4$, (*) $Li_{2/3}CoPO_4$, and (+) $LiCoPO_4$ [18].

Later Cycles: S/TEM-EELS Characterization

EELS Co L-edge Oxidation State Mapping

To confirm if a loss in capacity in charged $LiCoPO_4$ electrodes correlated to changes in the Co oxidation states and EELS Co L-edge shape, Co L-edges were extracted from the most Co(III)-rich regions of electrodes charged to 5.1 V vs. Li/ Li^+ after multiple cycles [18]. To find the most Co(III)-rich regions, oxidation state maps were generated using the standards in Figure *3*, and the EELS edges extracted from the areas MLLS fitting attributed to the Co(III)-rich standard.

The uncycled, and 1st cycle spectra are the same spectra as in *Figure 3*. The Co L_3 peak shifted from 781 to 782 eV on charging to 5.1 V vs. Li/ Li^+ on the first cycle, and the Co(II) multiplets disappeared on the Co L_3 and Co L_2-edges after charging to 5.1 V vs. Li/ Li^+ on the first cycle.

After 5 and 10 cycles Co L-edge spectra from electrodes charged to 5.1 V vs. Li/ Li^+ contain both Co(II)-rich and Co(III)-rich characteristics. Co(II) multiplets are observable on both the Co L_3, and Co L_2-edge of both the 5th, and 10th cycle Co L-edges (Figure *11*). The Co L-edge onset also occurs at the same energy loss as the uncycled Co(II)-rich standard for both the 5th and 10th cycle electrodes (779 eV). Despite these Co(II)-rich characteristics, the Co L_3-edge peak occurs at the same energy loss as the Co(III)-rich standard for both the 5th and 10th cycle electrode (782 eV).

The existence of mixed Co(II) and Co(III) characteristics for the EELS spectra from the charged 5th cycle electrodes correlates with a higher proportion of $Li_{2/3}CoPO_4$ measured by XRD, compared with the 1st cycle electrode (84.4 % and 41.9 % $Li_{2/3}CoPO_4$ after charging to 5.1 V vs. Li/Li^+ on the 1st and 5th cycles respectively).

The examined 10th cycle electrode had less Co(II) characteristics in the EELS Co L-edge (taken from the most Co(III)-rich regions) than the 5th cycle electrode (Figure *11*), which is unexpected. The results were consistent across 3 different areas of the samples. The differential capacity curves in Figure *9* show a lower capacity for the $LiCoPO_4$ after 10 cycles compared to 5 cycles, and the XRD patterns (Figure *10*) did not detect any Co(III) containing $Li_{2/3}CoPO_4$ or $CoPO_4$ after 10 cycles (which were detected in the 5th cycle XRD analysis).

This result suggests that after 10 cycles the Co(III) detected by EELS analysis is locally concentrated in delithiated compounds which are not overall detectable by XRD, due to low overall concentration or potentially lack of long range order [5], and which do not provide significant capacity contribution.

Co L-edge EELS spectra collected at different cycles

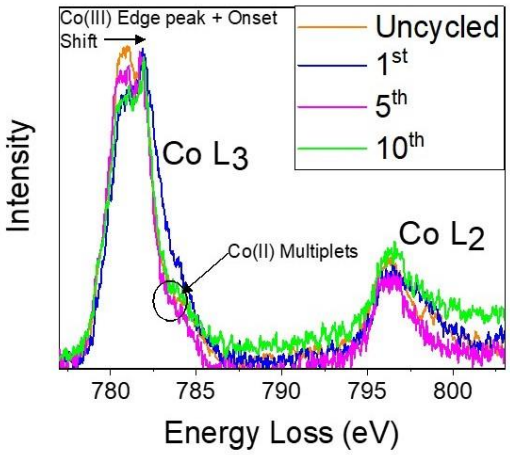

Figure 11: EELS Co L-edge spectra taken at a 0.025 eV/ ch energy dispersion of an uncycled $LiCoPO_4$ electrode (orange) and $LiCoPO_4$ electrodes charged to 5.1 V vs. Li/ Li^+ on the 1st cycle (blue), 5th cycle (pink), and 10th cycle (green). Co(II) multiplets occurred on the uncycled, 5th, and 10th cycle EELS spectra. The edge onset and peak of the Co L_3-edge EELS spectra with more Co(III) elements shift to higher energy losses. The EELS spectra have been rescaled so the maxima on the Co L_3 edge have the same intensity [18].

EELS O K-edge

A consequence of the shrinking core mechanism, with $CoPO_4$ forming initially on the particle outer surface and with associated Co-O hybridization, is that it is likely there will be O loss from $CoPO_4$, particularly as it forms near the particle/electrolyte interface. The presence of Co(II) on the surface of the particles at 4.98 V, and 5.1 V vs. Li/ Li^+ (above the breakdown potential of the electrolyte) in Figure *4* (h) and (j) is a further indicator of electrolyte induced damage.

To examine if the level of Co-O hybridization was affected on the 5th and 10th cycles by the increase in Co(II) characteristics within the Co(III)-rich regions of electrodes charged to 5.1 V vs. Li/ Li^+, O K-edges were compared (Figure *12*(a)). The O K-edges in Figure *12*(a) were taken with a 0.1 eV/ ch energy dispersion and are averages across the entire spectrum image (containing both Co(II) and Co(III)-rich regions). The O K-edge spectra were deconvolved to remove contributions from plural scattering.

Figure *12*(a) shows that for an uncycled electrode, no Co-O hybridization peak occurs, whereas for an electrode charged to 5.1 V vs. Li/ Li^+ on the 1st cycle, a Co-O hybridization peak occurs at 531 eV. The 1st cycle Co-O hybridization peak presented in Figure *12* has less relative intensity to the O K-edge than the hybridization peak of a similarly charged electrode in

Figure *6* because the O K-edge in Figure *12* also includes contributions from Co(II)-rich regions of sample, whereas the O K-edge in Figure *6* was extracted from Co(III)-rich regions only.

After cycling to 5.1 V vs. Li/ Li^+ on the 5th and 10th cycles, the O K-edge pre-edge peak is no longer present. The O K-edge shape of the charged 5th and 10th cycle electrodes is also identical to the uncycled electrode. The O K-edge was also examined for regions which mapped to Co(III)-rich by MLLS fitting (producing the Co L-edges in Figure *11*) on the 5th and 10th cycle (although not presented). No O K-edge pre-edge features were observed on any measured areas on the 5th and 10th cycle charged electrodes (sample maps are shown in Figure *12*(b).

The lack of O K pre-edge indicates no Co-O O-2p-Co-3d [8] bond hybridization at the 5th and 10th charge cycles. Reduced Co-O bond hybridization at later cycles occurs in conjunction with the Co L-edge containing more Co(II) characteristics at the 5th and 10th cycles (Figure *11*), consistent with the pre-edge being an indicator of Co(III)-rich regions (similar to the O K-edge in $Fe(III)PO_4$ [15]).

Maps showing how the presence of the O K-edge pre-edge compares with Co(II), and Co(III)-rich regions are also shown in Figure *12*(b-g). Similar to the maps in Figure *7*, the presence of the pre-edge peak on the O K-edge spectra correlates with the location of Co(III)-rich sample. The maps confirm the presence of the O K-edge pre-edge peak is consistent with the presence of Co(III), in a similar manner to $LiFePO_4$ [15]. The first cycle charged map shows that the particle surface, identified as Co(II)-rich, also lacks a pre-edge O K-edge feature, further confirming the surface of the particle is Co(II)-rich at high potentials.

It is likely no O-2p-Co-3d hybridization was observed at later cycles because the delithiation process is inhibited during later electrode cycles, resulting in significantly reduced Co(III) distribution. This is confirmed by the lack of $CoPO_4$ in the XRD patterns after 10 cycles in Figure *10*. Therefore, at later cycles, degradation resulted in an inability for $LiCoPO_4$ to delithiate.

Considering cathode degradation mechanisms, analysis of cycled $LiCoPO_4$ by Helium Ion Microscopy (HIM) and SIMS [21] indicates that the electrode particles undergo significant thickening of CEI layers with cycling, which can inhibit delithiation processes. Li-rich regions have also been found on the surface of charged $LiCoPO_4$ particles by SIMS [21], consistent with loss of capacity due to Li trapping in the CEI or reincorporation of Li into the structure [11]. Degradation may also be related to anti-site defect formation during prolonged cycling, described by Ikuhara *et al.* [7]. Anti-site defects cause blockages in the Li channels, preventing delithiation of $LiCoPO_4$ at later cycles, which may contribute to the reduction of Co(III)-rich regions at later cycles. Li K-edge mapping would be required to identify which mechanism has a greater effect on the degradation of $LiCoPO_4$.

For the shrinking core delithiation mechanism observed here (*Figure 5*), given that $CoPO_4$ (Co(III)) forms on the edge of $LiCoPO_4$ particles where it is more susceptible to electrolyte damage, and that the tendency for Co in $CoPO_4$ to hybridize with O indicates structural instability, efforts to improve the cyclability of $LiCoPO_4$ should focus on stabilizing the $CoPO_4$ phase.

O K-edge EELS spectra collected at different cycles

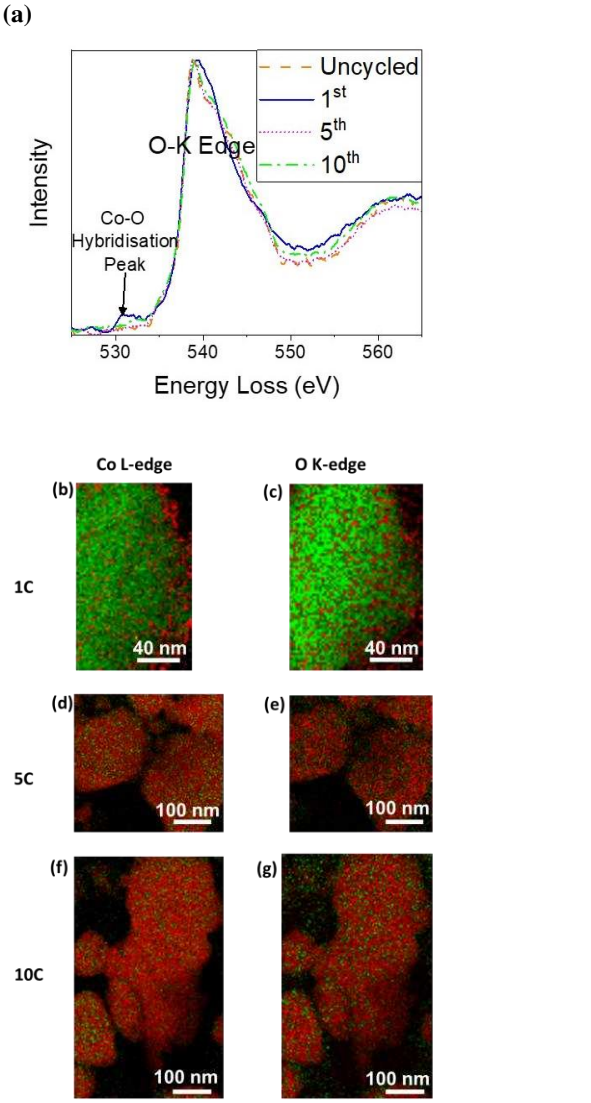

Figure 12: (a) EELS spectra of the O K-edge at a 0.1 eV/ ch energy dispersion of an uncycled $LiCoPO_4$ electrode (orange-dash-dot) and $LiCoPO_4$ electrodes charged to 5.1 V vs. Li/ Li^+ on the 1st cycle (blue-solid), 5th cycle (pink-dotted), and 10th cycle (green-dashed). The Co-O hybridization pre-peak and O K-edge are labelled. The EELS spectra have been re-scaled so the O K-edge peak has the same intensity. (b), (d), (f) Co L-edge and (c), (e), (g) O K-edge maps of particles charged to the 5.1 V vs. Li/ Li^+ on the (b), (c) 1st, (d), (e) 5th and (f), (g) 10th cycles labelled as 1C, 5C, and 10C respectively. Red regions on the Co L-edge maps represent Co(II)-rich regions, and green regions represent Co(III)-rich regions. Green regions on the O K-edge maps represent regions with a pre-edge, whilst red regions do not have an O K-edge pre-edge [18].

Conclusion

Co valence state EELS mapping has been used here to visualize the delithiation mechanisms of high voltage battery material, $LiCoPO_4$. The ability to spatially correlate the phases present during delithiation mapped by EELS with concurrent electrochemical behavior has found that Co(III)-rich regions, consistent with lithium poor regions, initially form on the surface of $LiCoPO_4$ particles. De-lithiation from the surface corroborates a shrinking-core mechanism previously identified through

in-situ XRD [14]. Eventually, the unstable Co(III)-rich, $CoPO_4$ phase forms on the surface of particles during delithiation. Co-O bonds hybridize via O-2p-Co-3d as a result of $CoPO_4$ formation. At higher potentials, a Co(II)-rich layer forms on the surface of the $LiCoPO_4$ particles. The presence of unstable $CoPO_4$, and associated O-2p-Co-3d hybridization on the surface of particles, leaves the Co(III)-rich phase formed open to attack from the electrolyte at high potentials, resulting in lithium re-incorporation at the surface, a Co(II)-rich surface and further capacity loss. Further cycling results in reduced Co-O hybridization and a more Co(II)-rich electronic structure, suggesting capacity is lost due to retained Li within the electrode structure. The results suggest strategies stabilizing the $CoPO_4$ phase, or shielding $CoPO_4$ from electrolyte attack and the associated consequences of Co-O hybridization could improve the cyclability of $LiCoPO_4$.

ASSOCIATED CONTENT

XRD refinement results; Co L-edge standards extraction method description; EELS Co L-edge Co(II) and Co(III)-rich standards; SAED and TEM images of the 5.1 V vs. Li/ Li^+ electrode; effect of air exposure on EELS Co L-edge; effect of microtoming on the EELS Co L-edge; representative galvanostatic charge and discharge curve of the $LiCoPO_4$ used here.

AUTHOR INFORMATION

Corresponding Author

* Laura Wheatcroft; l.j.wheatcroft@sheffield.ac.uk ; Department of Materials Science and Engineering, University of Sheffield, Mappin Street, Sheffield, UK S1 3JD

Author Contributions

The manuscript was written through contributions of all authors. / All authors have given approval to the final version of the manuscript.

Funding Sources

Engineering and Physical Sciences Research Council under grant EP/L016818/1.
Johnson Matthey

ACKNOWLEDGMENTS

The authors acknowledge Dr Manfred Schuster, Johnson Matthey Electron Microscopy for Microscope access at Harwell, Chris Hill, Biomedical Science Electron Microscopy Facility, The University of Sheffield for specimen preparation advice, staff at the Sorby Centre for Electron Microscopy, The University of Sheffield for assistance with TEM, and Johnson Matthey for providing the $LiCoPO_4$ powder. The Henry Royce Institute is thanked for funding time on the Panalytical Empyrean XRD, and JEOL JEM F200 TEM. The EPSRC under grant EP/L016818/1, the Energy Storage Centre for Doctoral Training at the University of Sheffield, and Johnson Matthey are thanked for a PhD studentship (L. Wheatcroft).

ABBREVIATIONS

S/TEM, scanning/ transmission electron microscopy; EELS, electron energy loss spectroscopy; SAED, selected area electron diffraction; XRD, X-ray diffraction; XAS, X-ray absorption spectroscopy

REFERENCES

(1) Bruce, P. G.; Freunberger, S. A.; Hardwick, L. J.; Tarascon, J. M. Li-O2 and Li-S Batteries with High Energy Storage. *Nature Materials*. Nature Publishing Group 2012, pp 19–29. https://doi.org/10.1038/nmat3191.

(2) Hu, M.; Pang, X.; Zhou, Z. Review Recent Progress in High-Voltage Lithium Ion Batteries. *Journal of Power Sources*. 2013, pp 229–242. https://doi.org/10.1016/j.jpowsour.2013.03.024.

(3) Amine, K.; Yasuda, H.; Yamachi, M. Olivine LiCoPO4 as 4.8 V Electrode Material for Lithium Batteries. *Electrochem. Solid-State Lett.* **2000**, *3* (4), 178–179. https://doi.org/10.1149/1.1390994.

(4) Zhang, M.; Garcia-Araez, N.; Hector, A. L. Understanding and Development of Olivine LiCoPO4 Cathode Materials for Lithium-Ion Batteries. *Journal of Materials Chemistry A*. Royal Society of Chemistry 2018, pp 14483–14517. https://doi.org/10.1039/c8ta04063j.

(5) Strobridge, F. C.; Clement, R. J.; Leskes, M.; Middlemiss, D. S.; Borkiewicz, O. J.; Wiaderek, K. M.; Chapman, K. W.; Chupas, P. J.; Grey, C. P. Identifying the Structure of the Intermediate, Li2/3CoPO4, Formed during Electrochemical Cycling of LiCoPO4. *Chem. Mater.* **2014**, *26* (21), 6193–6205. https://doi.org/10.1021/cm502680w.

(6) Bramnik, N. N.; Nikolowski, K.; Baehtz, C.; Bramnik, K. G.; Ehrenberg, H. Phase Transitions Occurring upon Lithium Insertion-Extraction of LiCoPO4. *Chem. Mater.* **2007**, *19* (4), 908–915. https://doi.org/10.1021/cm062246u.

(7) Ikuhara, Y. H.; Gao, X.; Fisher, C. A. J.; Kuwabara, A.; Moriwake, H.; Kohama, K.; Iba, H.; Ikuhara, Y. Atomic Level Changes during Capacity Fade in Highly Oriented Thin Films of Cathode Material LiCoPO4. *J. Mater. Chem. A* **2017**, *5* (19), 9329–9338. https://doi.org/10.1039/c6ta10084h.

(8) Lapping, J. G.; Delp, S. A.; Allen, J. L.; Allen, J. L.; Freeland, J. W.; Johannes, M. D.; Hu, L.; Tran, D. T.; Jow, T. R.; Cabana, J. Changes in Electronic Structure upon Li Deintercalation from LiCoPO $_4$ Derivatives. *Chem. Mater.* **2018**, *30* (6), 1898–1906. https://doi.org/10.1021/acs.chemmater.7b04739.

(9) Markevich, E.; Sharabi, R.; Gottlieb, H.; Borgel, V.; Fridman, K.; Salitra, G.; Aurbach, D.; Semrau, G.; Schmidt, M. A.; Schall, N.; Bruenig, C. Reasons for Capacity Fading of LiCoPO4 Cathodes in LiPF6 Containing Electrolyte Solutions. *Electrochem. commun.* **2012**, *15* (1), 22–25. https://doi.org/10.1016/j.elecom.2011.11.014.

(10) Manzi, J.; Brutti, S. Surface Chemistry on LiCoPO4 Electrodes in Lithium Cells: SEI Formation and Self-Discharge. *Electrochim. Acta* **2016**, *222*, 1839–1846. https://doi.org/10.1016/j.electacta.2016.11.175.

(11) Manzi, J.; Vitucci, F. M.; Paolone, A.; Trequattrini, F.; Di Lecce, D.; Panero, S.; Brutti, S. Analysis of the Self-Discharge Process in LiCoPO4 Electrodes: Bulks. *Electrochim. Acta* **2015**, *179*, 604–610. https://doi.org/10.1016/j.electacta.2015.03.071.

(12) Strobridge, F. C.; Liu, H.; Leskes, M.; Borkiewicz, O. J.; Wiaderek, K. M.; Chupas, P. J.; Chapman, K. W.; Grey, C. P. Unraveling the Complex Delithiation Mechanisms of Olivine-Type Cathode Materials, $LiFe_xCo_{1-x}PO_4$. *Chem. Mater.* **2016**, *28* (11), 3676–3690. https://doi.org/10.1021/acs.chemmater.6b00319.

(13) Kaus, M.; Issac, I.; Heinzmann, R.; Doyle, S.; Mangold, S.; Hahn, H.; Chakravadhanula, V. S. K.; Kübel, C.; Ehrenberg, H.; Indris, S. Electrochemical Delithiation/Relithiation of LiCoPO4: A Two-Step Reaction Mechanism Investigated by in Situ X-Ray Diffraction, in Situ X-Ray Absorption Spectroscopy, and Ex Situ 7Li/31P NMR Spectroscopy. *J. Phys. Chem. C* **2014**, *118* (31), 17279–17290. https://doi.org/10.1021/jp503306v.

(14) Palmer, M. G.; Frith, J. T.; Hector, A. L.; Lodge, A. W.; Owen, J. R.; Nicklin, C.; Rawle, J. In Situ Phase Behaviour of a High Capacity LiCoPO 4 Electrode during Constant or Pulsed Charge of a Lithium Cell. *Chem. Commun. Chem. Commun* **2016**, *52* (52), 14169–14172. https://doi.org/10.1039/c6cc07756k.

(15) Honda, Y.; Muto, S.; Tatsumi, K.; Kondo, H.; Horibuchi, K.; Kobayashi, T.; Sasaki, T. Microscopic Mechanism of Path-Dependence on Charge–Discharge History in Lithium Iron Phosphate Cathode Analysis Using Scanning Transmission

Electron Microscopy and Electron Energy-Loss Spectroscopy Spectral Imaging. *J. Power Sources* **2015**, *291*, 85–94. https://doi.org/10.1016/J.JPOWSOUR.2015.04.183.

(16) Sugar, J. D.; El Gabaly, F.; Chueh, W. C.; Fenton, K. R.; Tyliszczak, T.; Kotula, P. G.; Bartelt, N. C. High-Resolution Chemical Analysis on Cycled LiFePO4 Battery Electrodes Using Energy-Filtered Transmission Electron Microscopy. *J. Power Sources* **2014**, *246*, 512–521. https://doi.org/10.1016/J.JPOWSOUR.2013.08.003.

(17) Bramnik, N. N.; Bramnik, K. G.; Buhrmester, T.; Baehtz, C.; Ehrenberg, H.; Fuess, H. Electrochemical and Structural Study of LiCoPO4-Based Electrodes. *J. Solid State Electrochem.* **2004**, *8* (8), 558–564. https://doi.org/10.1007/s10008-004-0497-x.

(18) Structural Degradation Studies of High Voltage Lithium Ion Battery Materials - White Rose eTheses Online https://etheses.whiterose.ac.uk/28318/ (accessed Dec 15, 2021).

(19) Ehrenberg, H.; Bramnik, N. N.; Senyshyn, A.; Fuess, H. Crystal and Magnetic Structures of Electrochemically Delithiated Li1−xCoPO4 Phases. *Solid State Sci.* **2009**, *11* (1), 18–23. https://doi.org/10.1016/J.SOLIDSTATESCIENCES.2008.04.017.

(20) Mu, X.; Kobler, A.; Wang, D.; Chakravadhanula, V. S. K.; Schlabach, S.; Szabo, D. V; Norby, P.; Kubel, C. Comprehensive Analysis of TEM Methods for LiFePO4/FePO4 Phase Mapping: Spectroscopic Techniques (EFTEM, STEM-EELS) and STEM Diffraction Techniques (ACOM-TEM). *Ultramicroscopy* **2016**, *170*, 10–18. https://doi.org/10.1016/j.ultramic.2016.07.009.

(21) Wheatcroft, L.; Klingner, N.; Heller, R.; Hlawacek, G.; Ozkaya, D.; Cookson, J.; Inkson, B. J. Visualization and Chemical Characterization of the Cathode Electrolyte Interphase Using He-Ion Microscopy and *in-Situ* Time-of-Flight Secondary Ion Mass Spectroscopy. *ACS Appl. Energy Mater.* **2020**, acsaem.0c01333. https://doi.org/10.1021/acsaem.0c01333.